Proceedings of ASME Turbo Expo 2026
Turbomachinery Technical Conference and Exposition
GT2026
June 15-19, 2026, Milan, Italy

GT2026-176266

EXPERIMENTAL INVESTIGATION INTO SURGE BEHAVIOR OF TURBOCHARGER CENTRIFUGAL COMPRESSORS WITH LOCAL GEOMETRY VARIATIONS

Yiming Liu[1], Stephen Spence[1], George Sandford[2], Stuart Mann[2], Duncan McMath[2], Charles Stuart[1]

[1]Trinity College Dublin, Dublin, Ireland
[2]Cummins Components & Software, Huddersfield, UK

ABSTRACT

Surge is a flow instability phenomenon that limits the stable operating range of centrifugal compressors at low flow rates, posing a significant threat to compressor aerodynamic performance and safe operation. This paper presents an experimental study of surge behavior in three ported shroud equipped turbocharger centrifugal compressors with local geometry variations in ported shroud strut length and diffuser recess size. The experiments include the measurement of the stage performance map, interstage static pressure validation, and dynamic pressure characteristics during the throttling process towards surge boundaries. The results showed that even minor geometry variations in non-core components can significantly affect the compressor performance map width. Two distinct surge behaviors were identified: (i) TYPE A: the compressor experienced a surge island, characterized by mild surge, stability recovery, and deep surge eventually; (ii) TYPE B: the compressor directly evolved from mild surge into deep surge. The stability parameter (SP) of compressor sub-components was evaluated using a previously developed numerical model, revealing a strong correlation between impeller stability variation and the onset of mild surge. The underlying mechanism is that, as the flow rate reduces, a recirculating bubble is formed at the shroud side within the impeller exducer, which deteriorates impeller stability and triggers the onset of mild surge. The formation of the surge island is attributed to the partial removal of this recirculating bubble as it extends upstream to the ported shroud bleed slot with further flow rate reduction, which temporarily restores impeller stability and enables the compressor to recover from mild surge. To the best of the authors' knowledge, this study is the first to present the interaction between the recirculating bubble at impeller exducer shroud endwall and the ported shroud bleed slot, and to interpret the mechanisms of surge behaviors in ported shroud equipped centrifugal compressors. The research provides new insights for improving centrifugal compressor stability.

Keywords: Turbocharger Compressor; Ported Shroud; Surge Behavior; Experiment

NOMENCLATURE

Symbols

A_c	=	section area of the chamber (m^2)
CV	=	coefficient of variance
c	=	speed of sound (m/s)
c_{2u}	=	circumferential component of impeller outlet absolute velocity (m/s)
f_H	=	Helmholtz frequency (Hz)
IPF	=	impeller passing frequency (Hz)
L_c	=	length of chamber (m)
Ma	=	Mach number in relative frame
M_{u2}	=	impeller tip-speed Mach number
MFP	=	mass flow parameter (m·s·K$^{1/2}$)
p	=	static pressure (Pa)
Δp	=	inlet pressure differential (Pa)
SP	=	stability parameter
$u_{1,tip}$	=	peripheral velocity at impeller inlet tip (m/s)
u_2	=	peripheral velocity at impeller outlet (m/s)
V_p	=	volume of the plenum (m^3)
ρ	=	density (kg/m^3)
η	=	stage isentropic efficiency
μ	=	mean value
σ	=	standard deviation
ϕ	=	stage flow coefficient
ψ	=	static pressure rise coefficient

Abbreviation

B	=	baseline configuration
CFD	=	computational fluid dynamics

EXP	=	experiment
FFT	=	fast Fourier transform
M	=	million; modified struts configuration
MUA	=	measurement uncertainty analysis
MWE	=	map width enhancement
PRT	=	Platinum resistance thermometer
R	=	enlarged diffuser recess configuration
RANS	=	Reynolds-averaged Navier-Stokes
uRANS	=	unsteady Reynolds-averaged Navier-Stokes

Subscripts

00	=	throat of the converging nozzle for flow measurement upstream of the compressor
in	=	inlet of the sub-component
out	=	outlet of the sub-component

1. INTRODUCTION

Modern reciprocating engines are increasingly designed for compactness and high efficiency, making turbocharging an indispensable technology to improve both engine performance and fuel economy [1]. As the core component of a turbocharger, the centrifugal compressor plays a crucial role in determining the efficiency and performance of the engine. However, flow instabilities occur when the compressor operates at low mass flow rates, limiting its stable operating range. Especially when combined with complementary technologies such as Miller cycle, the result is an ongoing need for improving the performance and stability of the turbocharger compressor at low flow rate conditions [2]. Therefore, a comprehensive understanding of these flow instability phenomena is essential to ensure stable and reliable operation of turbocharger centrifugal compressors.

The most common flow instabilities in centrifugal compressors are rotating stall and surge. Rotating stall is local instability, which can occur in both impeller and diffuser. The stall cells typically propagate in the circumferential direction at a fraction of the rotor speed between 20% and 70% [3]. Rotating stall can lead to a pressure drop, but for centrifugal compressors, this pressure drop is usually not noticeable due to the centrifugal force and is therefore tolerable in most cases. Surge, on the other hand, is a system-level instability, characterized by global flow disturbances in the streamwise direction. Surge can be classified into mild surge and deep surge. Mild surge consists of small amplitude flow oscillations without net backflow, and its frequency typically corresponds to the Helmholtz frequency of the entire compression system. Whereas deep surge is when strong system oscillations occur with frequency of 3-10 Hz, including flow reversal through the compressor [4]. Deep surge is a damaging compressor operating regime and should be avoided.

Since surge is a system-level behavior, the investigations require consideration of the complete compression system. Greitzer [5] proposed a lumped parameter model to describe the dynamic characteristics of the compression system. B parameter was introduced to determine the onset of surge for a low-speed axial compressor. Hansen et al. [6] then applied this method to a centrifugal compressor. For numerical investigations, it is challenging to model the complex pipeline system. To address this, Zhang et al. [7,8] proposed a one-dimensional-three-dimensional coupled method to represent the one-dimensional flow in the pipelines of the compression system, and successfully demonstrated its capability in predicting the surge boundary of high-speed centrifugal compressors.

Most of the existing studies on centrifugal compressor surge behavior primarily relied on experimental approaches. Toyama et al. [9] and Dean et al. [10] measured the instantaneous pressure and velocity variations within a surge cycle of a centrifugal compressor using dynamic pressure transducers and hot-wire probes, making it a best practice for subsequent experimental studies. Zhao et al. [11] observed a quasi-linear relationship between the surge frequency and the compressor rotational speed. Such a quasi-linear relationship is not rare, but is not universally applicable. For example, it fails when the power source driving the compressor changes from an electric motor to a turbine. Manabe et al. [12] investigated the unsteady flow phenomena during the mild surge cycle in a transonic centrifugal compressor for an automotive turbocharger. The test confirmed that the rotating stall could coexist with mild surge in the vaneless diffuser. Zheng et al. [13–15] conducted a series of experimental tests on a small-scale high-speed turbocharger centrifugal compressor. Different compressor instability behavior was observed with the variation in impeller speed. At specific impeller speeds, a two-regime surge phenomenon can be observed, which features a non-surge region between the mild and deep surges [16,17]. Moreover, acoustic measurements are also employed in the experimental study of compressor surge. Zhao et al. [18] utilized microphones for surge detection. It was found that microphones have potential advantages for surge warning, since they are capable of identifying much weaker pressure fluctuations than dynamic pressure transducers. These studies have provided valuable insights into the surge behavior of centrifugal compressors.

A ported shroud is one of the passive flow control approaches to suppress flow instabilities and enhance compressor stability at low flow rates. It has been widely applied to turbocharger centrifugal compressors since its first implementation in the late 1980s [19]. The introduction of the ported shroud significantly changes the compressor internal flow field, resulting in a substantial influence on the compressor instability behavior [20]. Although numerous experimental studies have been conducted on turbocharger centrifugal compressors equipped with a ported shroud housing, most have focused on the validation of map width enhancement [21]. Limited tests have been performed to investigate the internal flow field and surge behavior. Tamaki [22] experimentally examined the unsteady flow phenomena in a centrifugal compressor equipped with a ported shroud, however the study focused on a large-scale low-speed compressor rather than a small-scale high-speed one.

This paper presents an experimental investigation on a turbocharger centrifugal compressor for a heavy-duty diesel application. The compressor is equipped with a ported shroud housing, and has three geometry configurations, which exhibit local geometry variations in non-core components. The aim of this study is to understand the surge behavior of these compressors and underlying mechanisms. As a start, the compressor geometry and experimental methodology are described in detail. Then, the test results are discussed in terms of performance map, interstage static pressure distribution and dynamic pressure characteristics. Finally, different compressor surge behaviors are analyzed, and the underlying mechanisms are interpreted with the aid of a previously developed numerical model.

2. METHODOLOGY

2.1. Compressor Configurations

The investigated turbocharger centrifugal compressor stage was for heavy-duty diesel applications, provided by Cummins Components and Software. The compressor stage has a ported shroud insert, an unshrouded impeller with seven main blades and seven splitter blades, a pinched vaneless diffuser, and a volute housing.

In addition to the baseline geometry (the B configuration), which features full-length ported shroud struts and a small size diffuser recess, the investigated compressor stage has another two geometry variants:

- M configuration with shortened ported shroud struts
- R configuration with a large size diffuser recess.

A schematic of all three geometry configurations is presented in Figure 1.

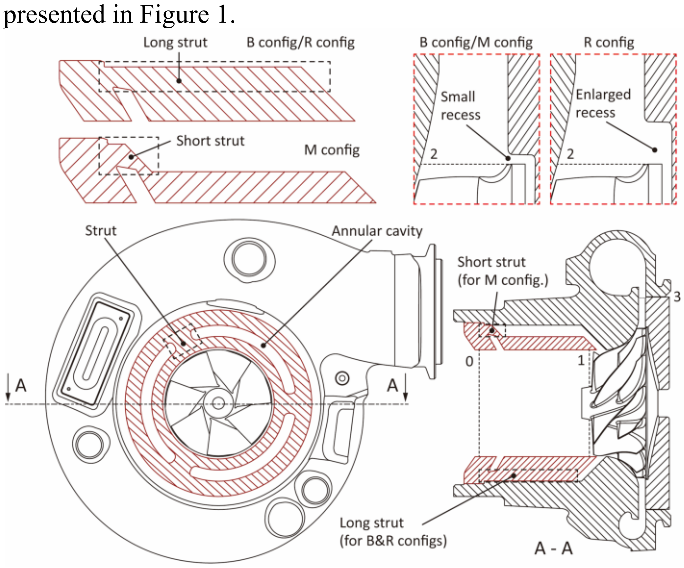

Figure 1: Schematic of three geometry configurations (not to scale)

2.2. Experimental Setup

The experimental campaigns consisted of two parts: the stage performance map tests and the internal flow field measurements. Both were conducted at the test facilities of Cummins Components & Software. Figure 2 shows the layout of the test rig. The Helmholtz frequency of the whole compression system was evaluated using a duct-plenum model [23–25]. The impeller passage was considered as the duct chamber, and all cavities between the impeller outlet and the boost valve (including diffuser, volute and downstream pipeline) were regarded as the plenum. The Helmholtz frequency f_{H} can be calculated as follows:

$$f_{\mathrm{H}} = \frac{c}{2\pi}\sqrt{\frac{A_{\mathrm{c}}}{L_{\mathrm{c}} \cdot V_{\mathrm{p}}}} = \frac{390}{2\pi}\sqrt{\frac{0.0001787}{0.0507 \times 0.064}} = 14.6\ \mathrm{Hz} \tag{1}$$

where c is the local speed of sound. Taking the average of the compressor inlet and outlet temperatures, c is approximately 390 m/s. A_{c} is the section area of one impeller outlet passage. L_{c} is the length of the impeller passage, which is estimated by the blade camber length at the mid-span location. V_{p} is the volume of the plenum. The Helmholtz frequency of the whole compression system was therefore calculated to be approximately 14.6 Hz.

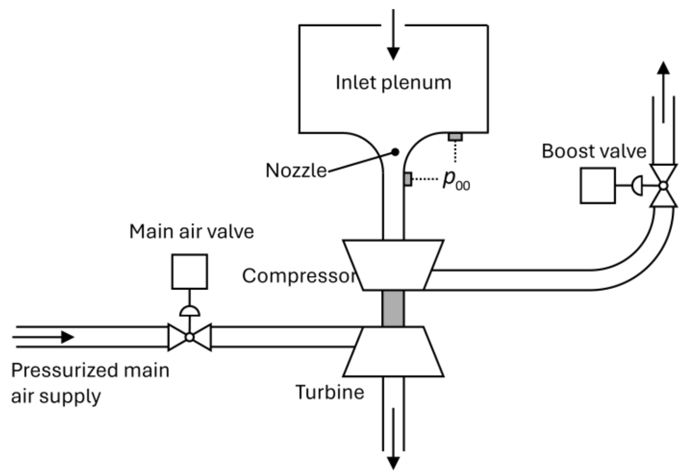

Figure 2: Schematic of test rig layout

The performance map measurements were conducted on a two-loop hot gas test stand in accordance with SAE J1826 Turbocharger Gas Stand Test Code [26]. The total pressure and total temperature at the compressor stage inlet and outlet were measured to calculate the total-total pressure ratio and total-total isentropic efficiency of the compressor stage. Class A Platinum Resistance Thermometers (PRTs) and Honeywell PPT series transducers were used for the measurements of total temperature and total pressure, respectively. The impeller rotating speed was measured using a magnetized nut system. The volumetric flow rate of the compressor stage was obtained by measuring the inlet differential pressure (Δp) across the nozzle located between the inlet plenum and the compressor stage, using a Honeywell PPT 0100 differential pressure transducer. In addition, the coefficient of variance (CV) of this inlet differential pressure (Δp) measured from a fast response differential pressure transducer UNIK 5000, was calculated for surge detection according to Eq. (2).

$$\mathrm{CV} = \frac{\sigma(\Delta p)}{\mu(\Delta p)} \times 100\% \tag{2}$$

where σ indicates the standard deviation, and μ implies the mean value. The CV value was calculated using a rolling window of 50 data, at a frequency of 25 Hz. Once the CV value of Δp increased beyond a preset threshold, then deep surge was considered to occur. More details of the test rig arrangements and surge measurement can be found in the previous study published by Cummins Components & Software [27].

Both interstage static pressure distribution and dynamic pressure signals were measured in the internal flow field tests. Two representative speedlines, 100% speed and 103% speed ($M_{u2} \approx 1.45$) were selected for the internal flow field tests, where significant stability difference can be observed (as depicted in Figure 4). Such a comparison therefore provided the ideal basis for subsequent analysis, through facilitating the clear mapping of changes in local flow structures to compressor sub-component and stage stability. A total of 24 measurement points were employed in the internal flow field tests, as illustrated in Figure 3. Among them, 20 static pressure taps were used in the steady-state "dwell tests", during which the compressor was operated steadily at fixed flow rate, to measure the static pressure distribution within the compressor, which covered various circumferential locations in the impeller exducer (1-1 to 1-8), diffuser (2-1 to 2-8) and volute (3-1 to 3-4). The pressure at each measurement location was transmitted through drilled ports on the volute housing to Druck PMP 4000 pressure transducers mounted in a switch box. The static pressure data were sampled at 1 Hz and averaged over a 10-second time window.

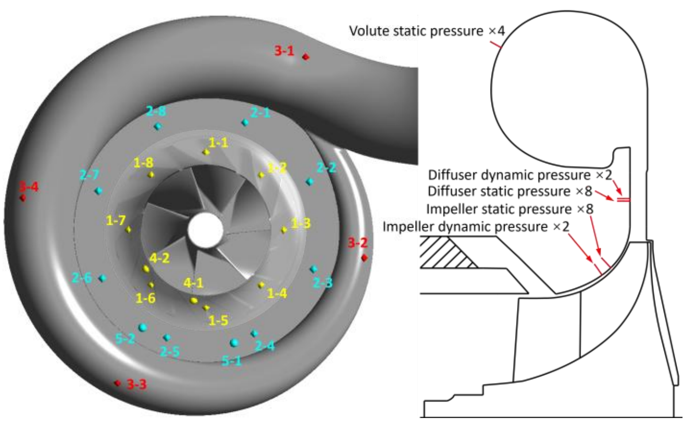

Figure 3: Schematic of pressure sensors setup

The remaining four measurement points were used to record dynamic pressure histories in the exducer (4-1 and 4-2) and diffuser (5-1 and 5-2) for the "sweep tests", during which the compressor was throttled from a high flow rate (e.g., S3 or S4 condition in Figure 4) towards the surge boundary. Kulite XCE-IC-093 sensors and Kulite XTEL-190SM sensors were employed at the exducer and the diffuser, respectively. The data acquisition system was DEWE-43V, which applied high-rate oversampling in MHz level and digital anti-aliasing filter prior to decimation. The final output data rate was 20 kS/s, which is more than ten times the impeller passing frequency (IPF), ensuring sufficient temporal resolution to capture potential instability phenomena within the compressor. The details of the measuring locations are summarised in Table 1. All the instrumentation employed in the experimental tests, together with their measurement uncertainty or MUA (Measurement Uncertainty Analysis) values, are summarised in Table 2.

Table 1: Summary of pressure sensor channels

Type	Channel No.	Location	Sensor
Static pressure distribution measurement	1-1	Exducer	Druck PMP 4000 (3.5 BarG)
	1-2		
	1-3		
	1-4		
	1-5		
	1-6		
	1-7		
	1-8		
	2-2	Diffuser	
	2-3		
	2-1		Druck PMP 4000 (4.5 BarG)
	2-4		
	2-5		
	2-6		
	2-7		
	2-8		
	3-1	Volute	
	3-2		
	3-3		
	3-4		
Dynamic pressure measurement	4-1	Exducer	Kulite XCE-IC-093 (50 psiA)
	4-2		
	5-1	Diffuser	Kulite XTEL-190SM (60 psiA)
	5-2		

Table 2: Summary of instrumentation

Measured parameter	Sensor	Uncertainty/ MUA value
Shaft speed	Magnetized nut	±0.068 rpm
Pressure differential for flow rate	Honeywell PPT 0100	±0.05% full scale
Pressure differential for surge detection	Unik 5000	±0.2% full scale
Compressor inlet total temperature	Class A PRT	±0.35 °C
Compressor outlet total temperature	Class A PRT	±0.5~±0.7°C
Compressor inlet total pressure	Honeywell PPT 0100	±1.46 mbar
Compressor outlet total pressure	Honeywell PPT 0100	±5 mbar
Interstage static pressure	Druck PMP 4000	±0.04% full scale
Dynamic pressure	Kulite XCE-IC-093; Kulite XTEL-190SM	±0.1% full scale

3. EXPERIMENTAL RESULTS AND DISCUSSION

3.1. Performance Map

The measured stage performance map of all three compressor configurations is shown in Figure 4. The mass flow parameter (MFP) values were normalized to the choke value of the B configuration at 100% speed.

The geometries of these three compressor configurations are broadly similar (sharing the same impeller, diffuser radius ratio and volute geometry), leading to the expectation of comparable performance at the design point. This expectation was confirmed by experimental measurements of the stage total pressure ratio and isentropic efficiency. However, notable differences in stability were observed among these three configurations. These differences are believed to stem from minor geometric variations, such as the shape of ported shroud struts and the size of the diffuser recess (as referenced in relation to Figure 1). Previous simulation work indicated that the enlarged diffuser recess of the R configuration alleviated flow separation within the vaneless diffuser, thereby resulting in the widest performance map. Furthermore, the shortened struts of the M configuration induced positive pre-swirl into the recirculating flow from the ported shroud channel, reducing the impeller blade loading and consequently resulting in the worst stage stability among the three geometry configurations [28,29].

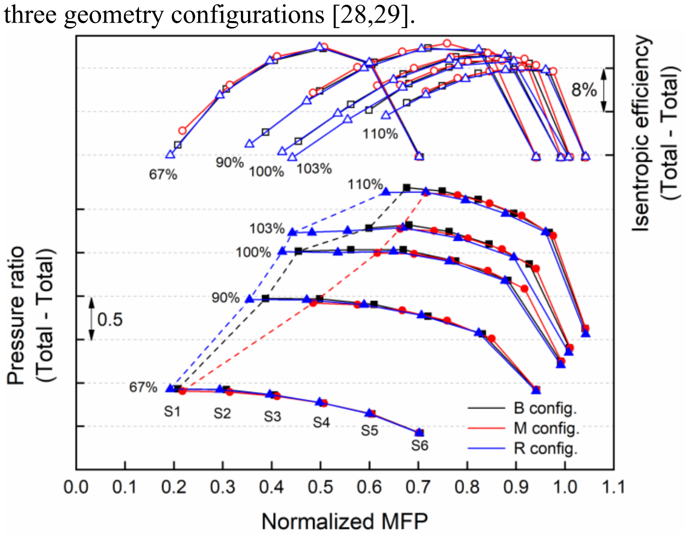

Figure 4: Compressor stage performance map from tests

In order to clearly describe the operating conditions of different compressor geometry configurations, a naming convention was derived, e.g., B_103%_0.60. Here B denotes the baseline B configuration. The shortened struts M configuration and the enlarged diffuser recess R configuration are represented by M and R, respectively. 103% indicates the operating speedline, and 0.60 refers to the normalized MFP. Moreover, the operating conditions along each speedline were noted as S1 to S6, where S1 corresponds to the last stable operating point before entering deep surge and S6 to the choke point.

3.2. Static Pressure Validation

The time-averaged static pressure distribution within the compressor stage is presented in Figure 5. Only the results of B_100%_0.55 (S2 condition) are shown as a representative case for brevity. The CFD results obtained from the previously developed high-fidelity unsteady numerical model are also included in the figure to validate the accuracy and reliability of this numerical model. The numerical model is shown in Figure 6, and its main features are summarised in Table 3. More details of this numerical model are available in the authors' previous studies [28,30].

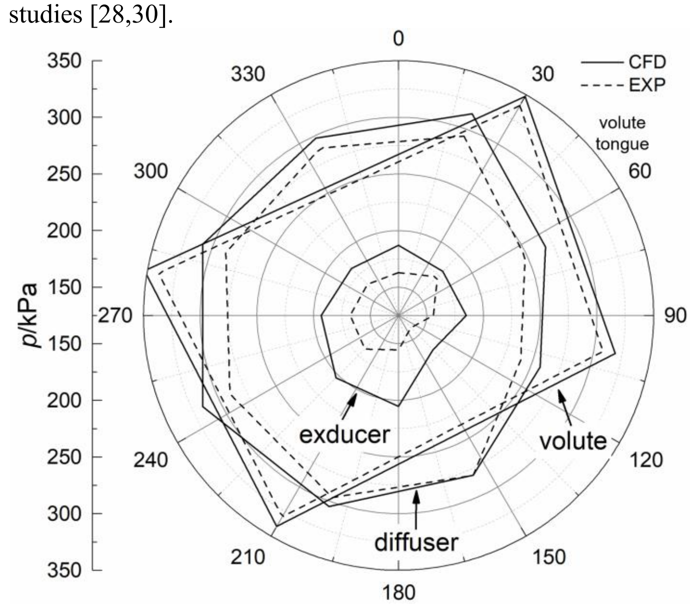

Figure 5: Interstage static pressure validation for B_100%_0.55 (S2 condition)

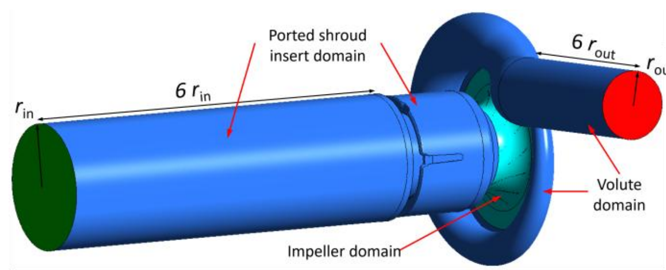

Figure 6: Numerical model of the B configuration

Table 3: Summary of the numerical model

Item	Description
Solver	ANSYS CFX 2021R1
Governing equations	RANS/uRANS
Turbulence model	SST k-ω with reattachment modification
Computational domain	Full annulus
Interface type	Frozen rotor (steady) Transient rotor stator (unsteady)
Mesh size	20.5 million nodes (B config.)

The numerically predicted static pressure distribution exhibited a high level of agreement with the experimental test results. The CFD predictions were slightly higher than the experimental measurements, which may be attributed to the limitations of the numerical model, such as the assumptions of the turbulence model. The difference between the CFD predictions and experimental measurements became smaller as the flow progressed downstream. At the impeller exducer, the CFD predicted static pressure was on average 17.2% higher than the experimental measurements, while the deviations reduced to 5.7% in the diffuser and 3.2% in the volute, as summarised in Table 4. Therefore, it is suggested that further experimental validation work should preferably measure static pressure distribution at downstream locations, e.g., within the diffuser or volute, where the CFD predictions and experimental measurements had better agreement. The trend in terms of circumferential distortion induced by the volute tongue was also well captured. This validated the accuracy and reliability of the previously developed CFD model, which will also be employed in the subsequent analysis for interpretation of the experimental observations.

Table 4: Average deviation of interstage static pressure between CFD and experiment for B_100%_0.55

	Impeller	Diffuser	Volute
Absolute	27.3 kPa	15.6 kPa	10.6 kPa
Relative	17.2%	5.7%	3.2%

3.3. Dynamic Pressure Analysis

Dynamic pressure measurements from all four Kulite sensors were analysed to investigate flow instability behavior of the studied compressor stages. Fast Fourier Transform (FFT) was employed to examine the characteristics of dynamic pressure signals in the frequency domain. A sliding window of two seconds with 75% overlap ratio was applied, which provided a frequency resolution of 0.5 Hz and enables a clearer identification of low-frequency flow instability features. The Hann window technique [31] was employed to reduce spectral leakage. The raw data were centered to eliminate the influence of direct current component and reduce interference with low-frequency signals.

Figure **7** illustrates the spectrograms of dynamic pressure signals recorded by all four Kulite sensors during the “sweep test” for the B configuration on 100% speedline. The spectrogram captures the temporal evolution of signal frequency and can indicate the instability behavior. The results indicated that the frequency characteristics of pressure signals from all four Kulite sensors were broadly similar. Probe 5-2 exhibited the clearest frequency components and was thus selected for detailed frequency-domain analysis.

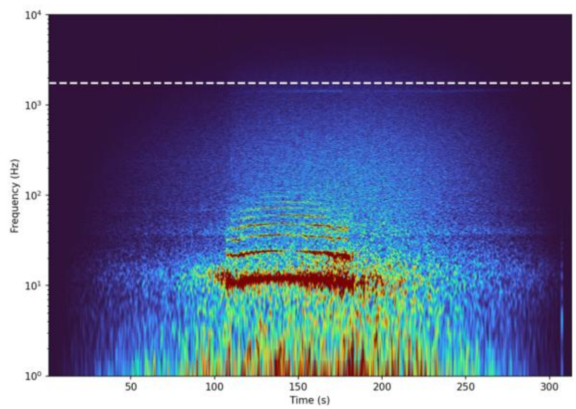

(a) Probe 4-1

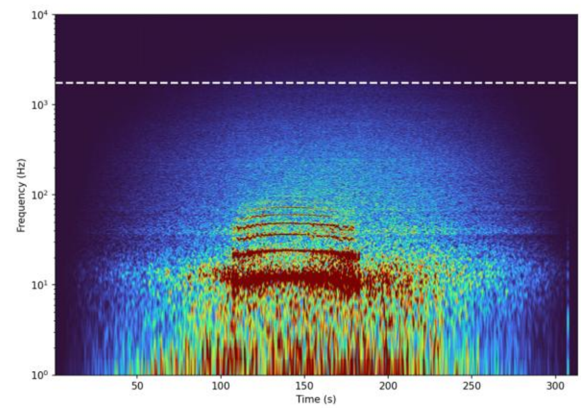

(b) Probe 4-2

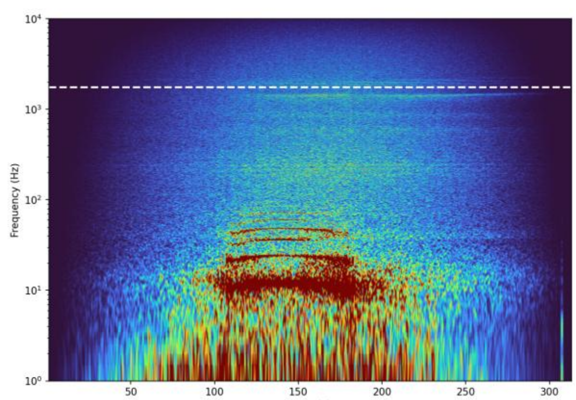

(c) Probe 5-1

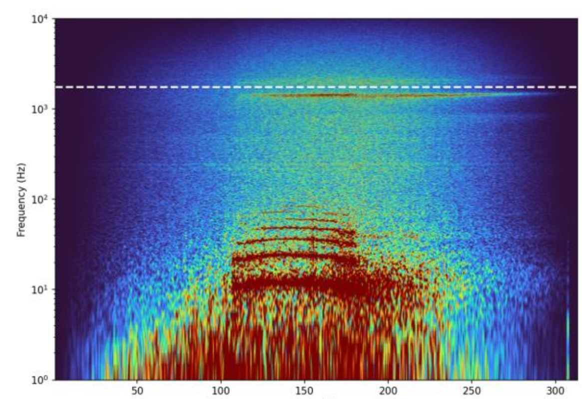

(d) Probe 5-2

Figure 7: Spectrogram of all four locations of B_100%

Figure 8 presents the spectrograms of probe 5-2 for all three geometry configurations. The x-axis denotes the real time during the throttling process of the “sweep test”. The B configuration on 100% speedline (Figure 8(a)) was analysed first. The “sweep test” began at a relatively high mass flow rate condition (around S3 condition), and the control system gradually closed the boost valve to throttle the compressor towards surge. At approximately 105 s, a significant low-frequency signal ① (~12 Hz) and its harmonics were observed. This frequency was close to the Helmholtz frequency of the whole compression system (~14.6 Hz), indicating the onset of the mild surge. As the throttling process continued, the mild surge disappeared at around 220 s, and the compressor temporarily returned to a stable condition. Eventually, the compressor abruptly entered deep surge ② at around 307 s. Since the control system opened the boost valve quickly once the compressor entered deep surge to protect the hardware, only one to three complete surge cycles could be captured during the “sweep test”, resulting in a relatively narrow deep surge signal band. The frequency of the deep surge signal was below 5 Hz, which was consistent with the compression system deep surge characteristics. This flow behavior, characterized by mild surge followed by a temporarily stable state, is referred to as “surge island” or “two-regime surge” [16,17,32], which is often observed in small centrifugal compressors. This instability behavior was also observed in R_100% (Figure 8(c)) and R_103% (Figure 8(f)).

In addition, a high-frequency signal ③ with large amplitude was observed at approximately 80% IPF. This signal began concurrently with the onset of the mild surge and persisted until the onset of deep surge. Notably, the high-frequency signal persisted beyond the end of the surge island, although the signal amplitude was slightly reduced. The frequency of this signal fell outside the typical range of the rotating stall in centrifugal compressors (20%-70% IPF) [33]. To further investigate this signal, Figure 9 shows the pressure traces from the two Kulite sensors mounted in the diffuser (Probe 5-1 and Probe 5-2) when operating within the surge island for B_100%. A band-pass filter of 55%-115% IPF was applied to isolate the frequency components near 80% IPF. No clear phase difference was observed between two pressure traces, suggesting that this high-frequency signal was not rotating stall. It was probable that this high-frequency signal was the vortex shedding from impeller trailing edge, which was referred to as high-frequency stall and confirmed by Zheng and Liu [13].

When the impeller of the B configuration was accelerated to 103% speed (Figure 8(d)), the compressor exhibited a different instability behavior. The compressor entered mild surge at around 95 s, which persisted until deep surge occurred (④). Similarly, the high-frequency stall signal ③ near 80% IPF was also observed. It appeared with the onset of the mild surge and continued until the occurrence of deep surge. This instability behavior was also observed in M_100% (Figure 8(b)) and M_103% (Figure 8(e)). However, the mild surge duration is shorter at these two conditions, and the high-frequency stall signal is less evident. It is noted that for M_103% (Figure 8(e)), the duration of the mild surge event was very short, making it

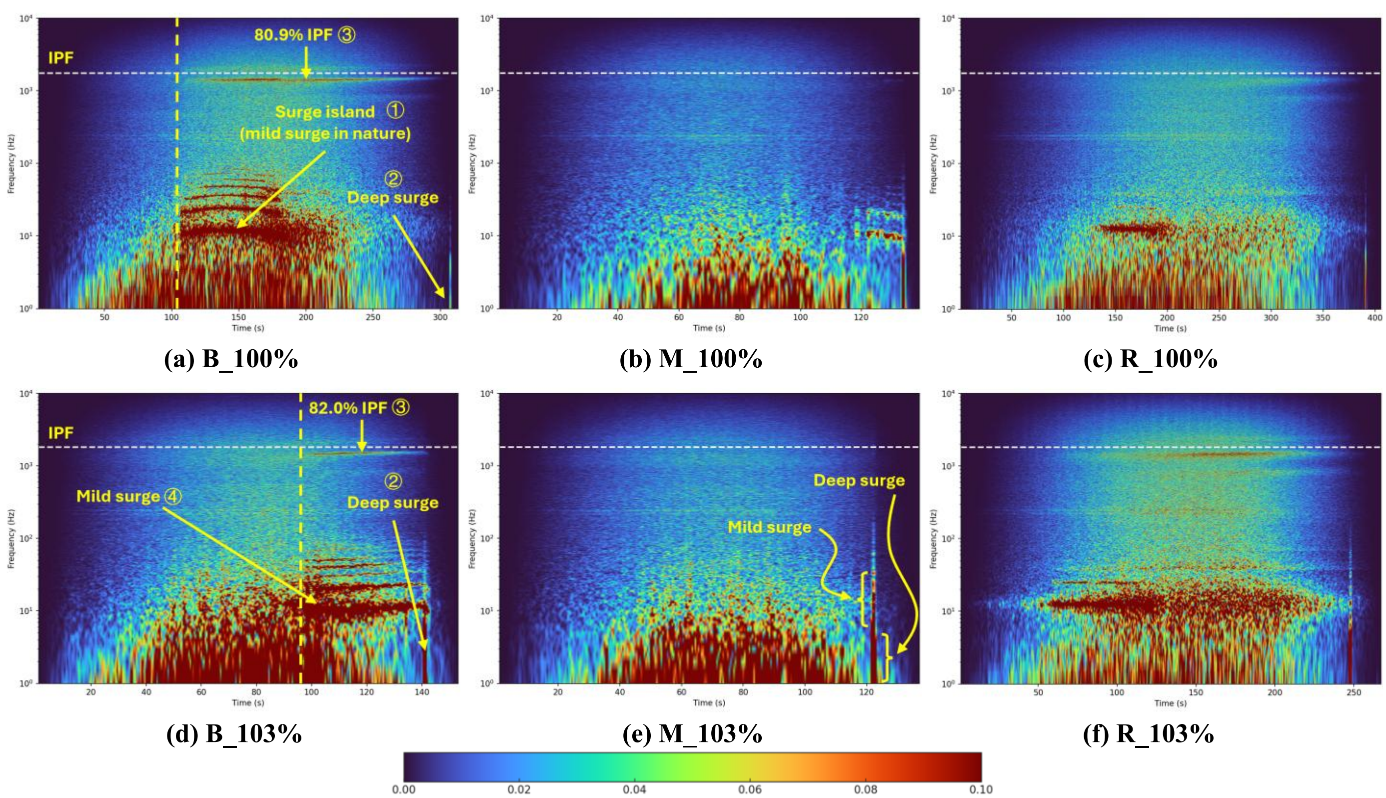

Figure 8: Spectrogram of dynamic pressure taken at probe 5-2

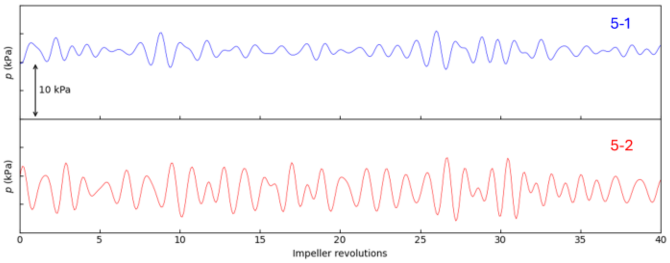

Figure 9: Pressure traces in the diffuser of B_100% when operating within the surge island

difficult to distinguish the mild surge signal from the deep surge signal. However, the presence of frequency components higher than 12 Hz indicated that the mild surge indeed occurred for M_103%.

In summary, there were two instability behaviors identified in the studied three compressor stages:

- TYPE A: The compressor enters mild surge first, and then recovers to a stable state temporarily (namely surge island). Eventually, the compressor enters deep surge abruptly (Figure 8(a), Figure 8(c), and Figure 8(f)).
- TYPE B: The compressor enters mild surge, which persists continuously until the occurrence of the deep surge (Figure 8(b), Figure 8(d), and Figure 8(e)).

Although these two instability behaviors differed in the process leading to surge, a common characteristic was that no rotating stall was observed prior to the event of mild surge or deep surge. This observation is consistent with the findings by Toyama et al. [9], i.e., for some small centrifugal compressors, rotating stall may not occur and the compressor will transition directly into surge. Zheng et al. [13–15] also confirmed that this phenomenon tended to occur at high rotating speeds ($M_{\mathrm{u2}} \approx 1.50$). Figure 10 summarizes the compressor instability behavior of all three geometry configurations overlaid on the compressor performance maps.

3.4. Pressure Variations in Surge Cycles

In addition to the frequency domain characteristics, the time domain features of the dynamic pressure signals were also analysed. Figure 11 summarizes dynamic pressure signals recorded by all four Kulite sensors before and after the event of the deep surge for all three geometry configurations.

It can be observed that pressure fluctuations within the diffuser were more significant compared to those within the impeller. For cases exhibiting TYPE B instability behavior, e.g., B_103% (Figure 11(d)), large-scale pressure oscillations were detected by all Kulite sensors before and after the event of the deep surge. The oscillation period of one complete mild surge cycle was approximately 0.083 s, which aligned with the frequency of mild surge signal (~12 Hz) detected in spectrograms shown in Figure 8. During the deep surge cycle, impeller pressure exhibited a significant “double peak” pattern. The diffuser pressure exhibited a small rise before the pressure collapsed. However, both pressure rise and drop phases demonstrated a non-monotonic, wave-like behavior. This was characterized by a series of small-scale pressure oscillations superimposed on the overall variation trend, which was more clearly observed for diffuser pressure. The period of a complete deep surge cycle was approximately 0.235 s, corresponding to a deep surge frequency of about 4.2 Hz.

The pressure evolution within the impeller and the diffuser in different phases during one complete deep surge cycle is illustrated in Figure 12, using B_100% as an example.

At time instant 1, the compressor was about to enter deep surge. As the downstream pressure of the compressor gradually increased, the impeller was unable to provide sufficient momentum to the flow to overcome the high adverse pressure gradient within the compressor, causing the flow to progressively stagnate and the static pressure to rise. As a result, local static pressure rise can be observed within both the impeller and the diffuser. Moreover, the mass flow rate reduced rapidly during this period, resulting in a reduced impeller power. Since the driven power provided by the turbine remained constant over a short period of time, the shaft speed began to increase as shown in Figure 13. Although the backswept blades employed in the studied compressor tended to increase $c_{2\mathrm{u}}$ as the flow rate decreased [34] and the rise in impeller shaft speed increase u_2, the reduction in flow was substantial rather than a small perturbation (flow rate reduced sharply and may even cause backflow later). Consequently, the effect of the variation in impeller Euler work was much smaller than that of the influence

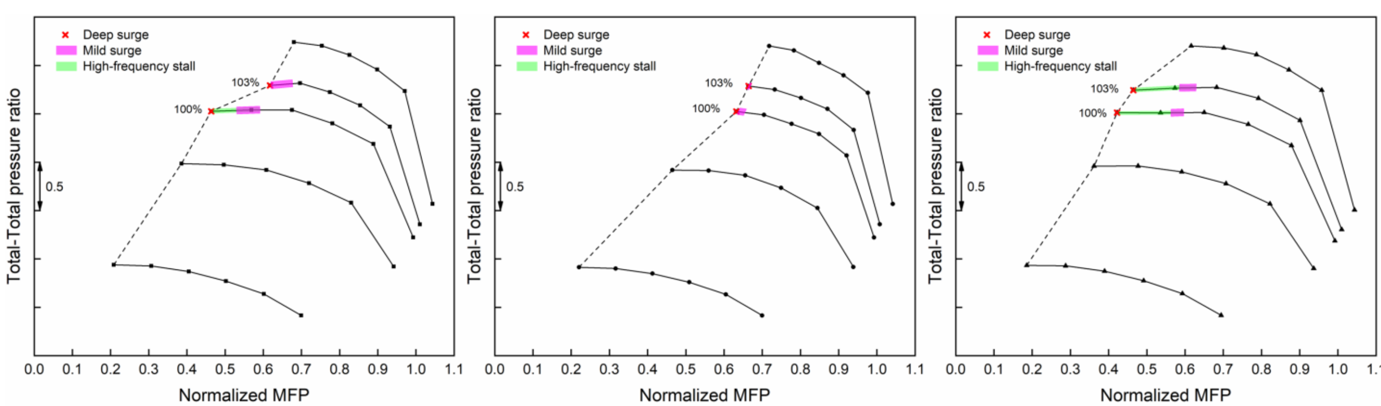

(a) B configuration **(b) M configuration** **(c) R configuration**

Figure 10: Performance map overlaid with compressor instability behavior

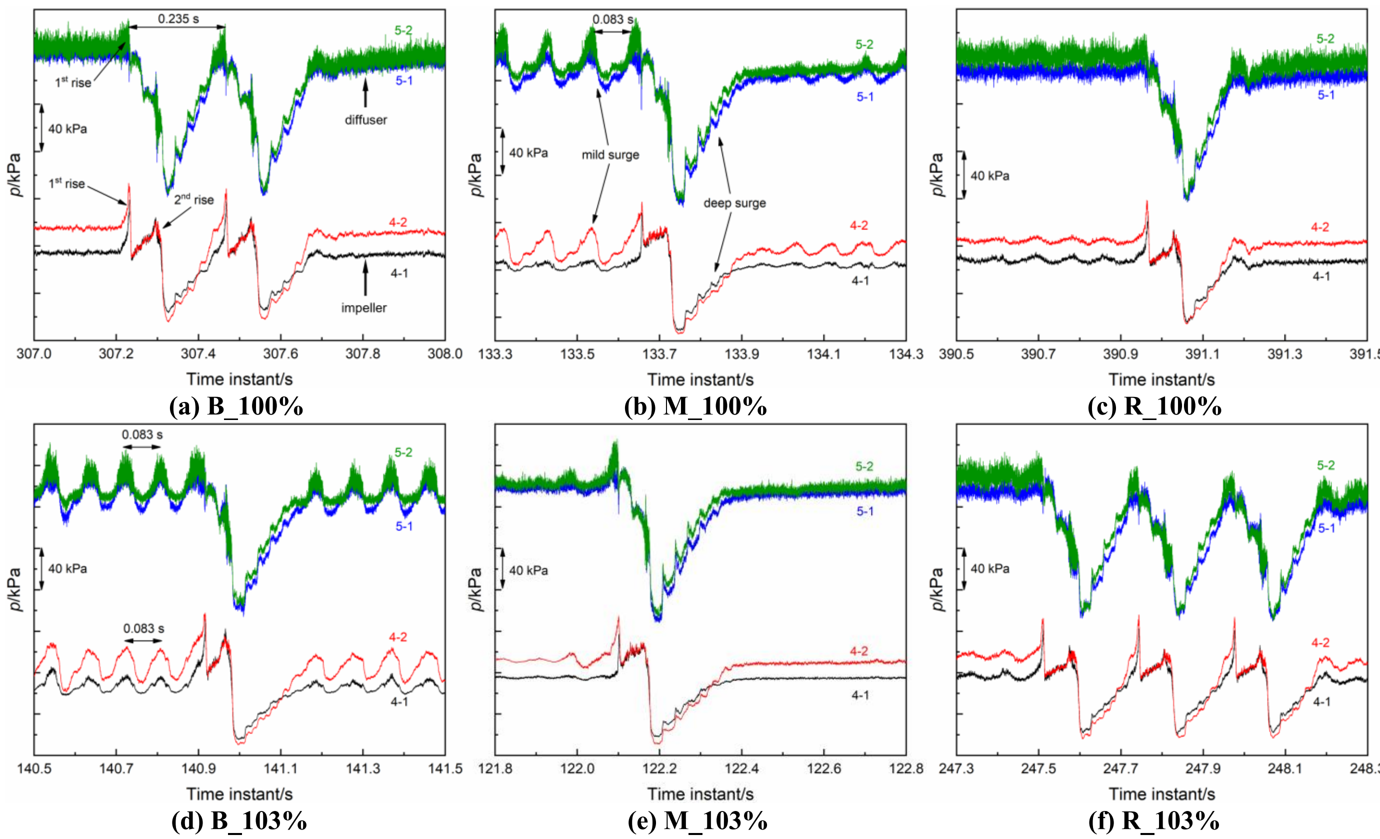

Figure 11: Dynamic pressure history in the vicinity of the deep surge

of flow rate reduction. Toyama et al. [9] attributed this local pressure rise prior to the onset of the surge to the disturbance in the system mass flow rate

During phase 2-3, the pressure within the impeller and the diffuser experienced a sudden drop, which was generally regarded as the onset of deep surge, as well as the initiation of the backflow [9].

In phase 3-5, the continuous increase in impeller shaft speed resulted in an enhancement of impeller boosting capability. Additionally, combined with the reduced impeller back pressure, it allowed the impeller to temporarily regain forward flow and to boost again. This led to a 2nd pressure rise and formed the 2nd peak of the impeller "double peak" pattern. However, backflow and pressure collapse persisted in the diffuser, indicating that the investigated compressor stages exhibited complex local backflow rather than a global backflow during these phases. Notably, during these phases, pressure at different circumferential locations exhibited almost the same magnitude, indicating that the pressure field was not affected by the circumferential distortion induced by the volute tongue during the deep surge cycle. This also implied that the local backflow redistributed the flow field downstream of the impeller, mitigating the circumferential distortion effect induced by the volute tongue. It should also be noted that significant fluctuations in impeller shaft speed occurred in this stage, indicating that the impeller flow rate had large oscillations.

In phase 5-6, after reaching the 2nd peak, the impeller pressure failed to maintain the high pressure and the local backflow within the impeller occurred again, leading to another pressure collapse. The pressure in both components dropped sharply, reaching their respective minimum.

After time instant 6, the downstream pressure was at its minimum and the impeller shaft speed at its maximum. The positive flow was reestablished. The impeller boosting capacity was regained and the whole compression system began to compress, until the pressure returned to the nominal value associated with the operating condition, signifying the completion of a deep surge cycle at time instant 8.

Figure 14 presents the evolution of some flow parameters during the throttling process towards surge, starting from the S4 condition. During the surge island regime, the inlet Δp exhibited significant fluctuations, with the CV of inlet Δp rising to approximately 30%, yet remaining below the predefined threshold (40%-45%). With the flow rate further reduced, the surge island disappeared, and the inlet Δp fluctuations returned to the normal level. When deep surge occurred, the inlet Δp decreased significantly and even became negative. This clearly indicated that the reduction of the flow rate or the backflow had propagated to the compressor inlet. Because the mass flow rate was measured at a relatively low frequency, i.e., 1 Hz, the temporal resolution was not enough to resolve the instantaneous change in flow rate when deep surge occurred.

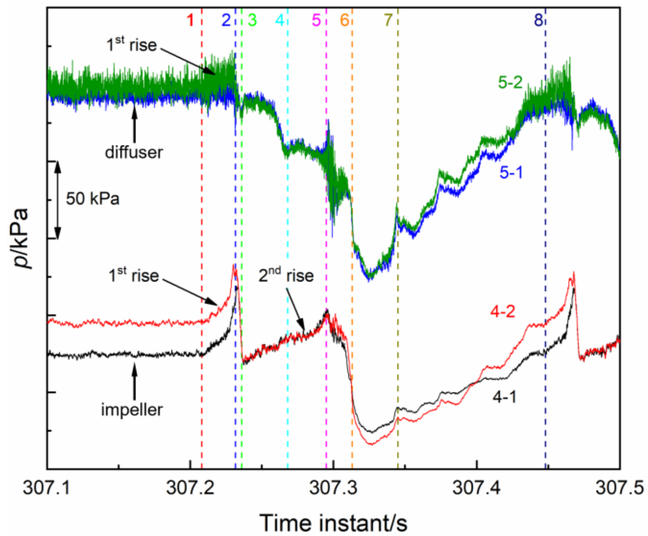

Figure 12: Pressure variations in one complete deep surge cycle of B_100%

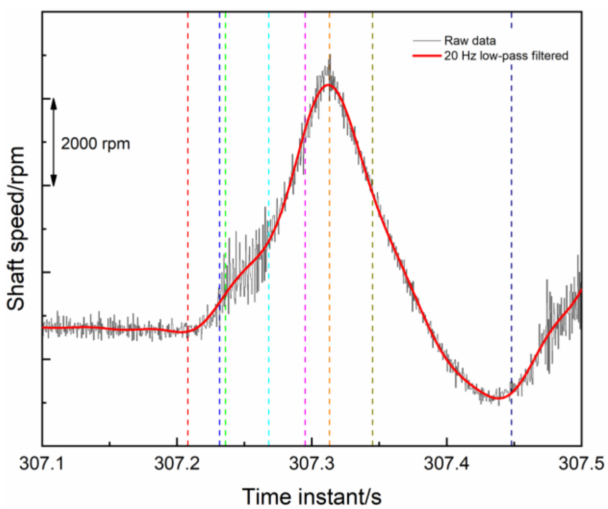

Figure 13: Impeller shaft speed in a complete deep surge of B_100%

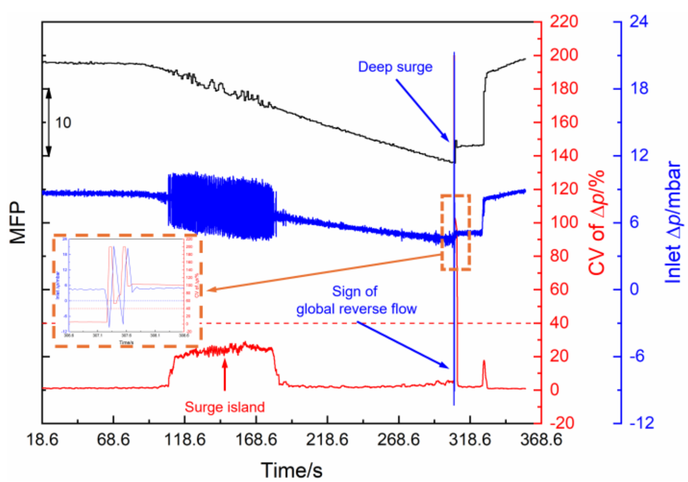

Figure 14: Flow parameters of the "sweep test" for B_100%

4. MECHANISMS OF SURGE BEHAVIOR

4.1. Components Stability Characteristics

The stability parameter (SP) proposed by Dean [35] and Japikse [36] was applied to analyse the stability of different sub-components of the studied compressor stages. The definition of SP is shown as the following formula:

$$\mathrm{SP} = \frac{\mathrm{d}(\psi_{\mathrm{out}} - \psi_{\mathrm{in}})}{\mathrm{d}\phi} \cdot \frac{1}{|\psi_{\mathrm{out}}|} \tag{3}$$

where ψ represents the static pressure rise coefficient and ϕ denotes stage inlet flow coefficient. The subscript "out" and "in" refer to the location of the outlet and inlet of each sub-component. The SP values of the impeller, the diffuser, the volute and the whole stage were calculated and analysed. The static pressure rise coefficient ψ at each section plane is defined as:

$$\psi_i = \frac{p_i - p_\infty}{\frac{1}{2}\rho_\infty u_{1,\mathrm{tip}}^2} \tag{4}$$

where the reference static pressure at infinity is atmospheric pressure, i.e., $p_\infty = 101325$ Pa, and the reference air density at infinity is taken as $\rho_\infty = 1.225\ \mathrm{kg/m^3}$. The subscript *i* indicates different measuring locations.

Stability parameter is actually the gradient of the pressure rise coefficient ψ against the stage inlet flow coefficient ϕ. If the SP value is smaller than zero, this means that the pressure rise coefficient curve has a negative slope, indicating a stable state; if the SP value is greater than zero, the pressure rise coefficient curve has a positive slope, which implies an unstable state.

Figure 15 shows the SP values for different sub-components evaluated from the previously developed high-fidelity, unsteady CFD model [28,30]. The static pressure at each measurement location was area-averaged from CFD results. All diagrams show that the stage SP value became positive at the S3 or S2 condition, suggesting the onset of the whole stage instability. However, this did not imply that the compressor stage was critically destabilized. In fact, all the operating points presented in the diagrams were measured to be globally stable in the experimental tests, with the S1 condition representing the last stable operating point prior to entering deep surge. The stable operating of the compressor stage depended not only on the stage SP value, but also on the coupling with the upstream and downstream pipeline system. This underscored the limitation of using the stage SP value or the slope of the static pressure rise curve as an absolute indicator of compressor instability.

As the mass flow rate reduced, the diffuser was the first component to become unstable, primarily due to the instability within the parallel wall section, which remained unstable across nearly the entire flow range. The diffuser became most unstable around the S3 condition, after which its stability improved, but remained unstable. Then the volute became unstable, followed by the whole stage. The impeller was the last component to exhibit stability turnover. It was noted that the impeller was almost stable across the entire operating map, which could be attributed to the introduction of the ported shroud. Other studies have reported different findings. Liu et al. [37] and Hunziker et

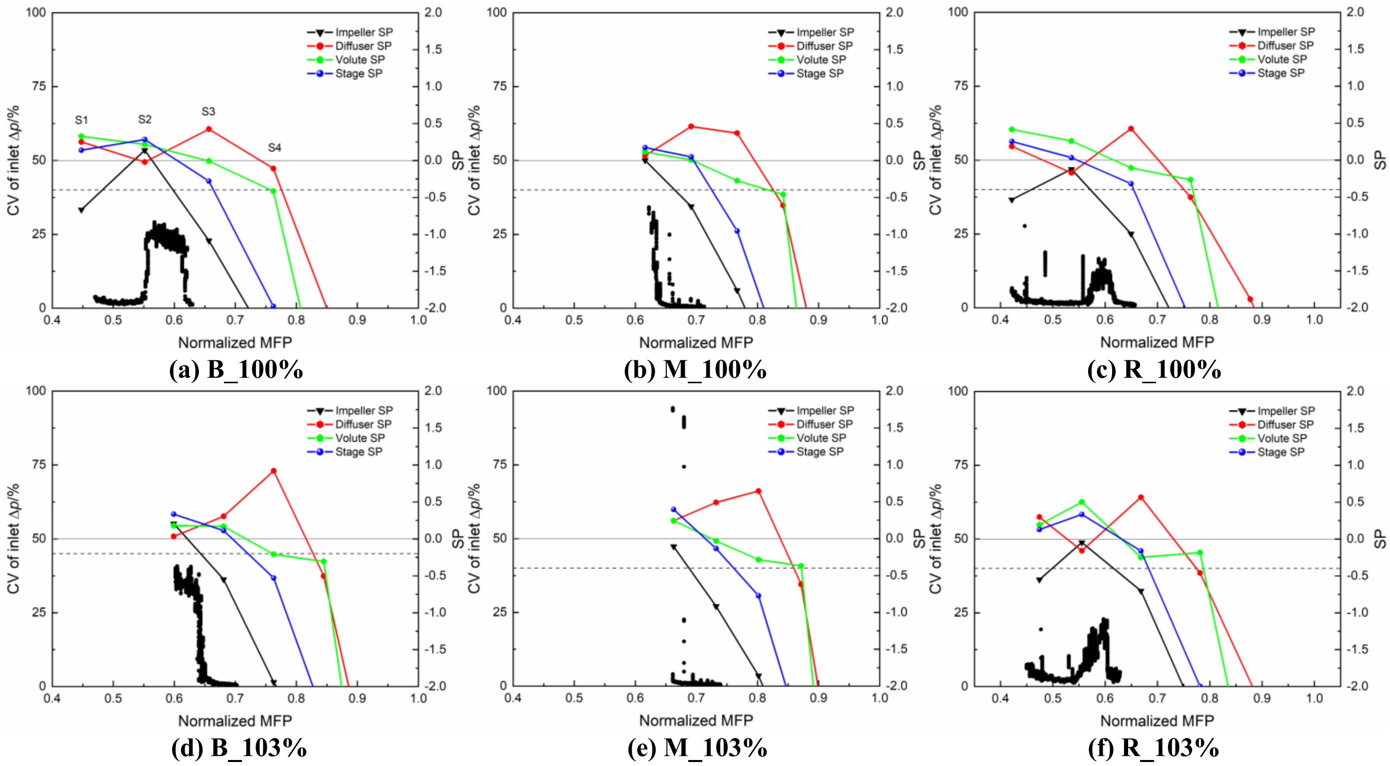

Figure 15: Correlation between stability parameters and the onset of mild surge

al. [38] demonstrated that the impeller was the primary source of instability, while the diffuser provided a stabilizing effect. However, the diffusers used in those studies were vaned configurations. Nevertheless, these investigations also provided some useful insights into compressor instability, which highlighted that the source of compressor instability varied from case to case, indicating highly complex underlying mechanisms.

Two distinct patterns of the impeller SP curves were observed. The first was that the impeller gradually became unstable as the flow rate decreased until reaching the surge boundary, as shown in Figure 15(b), Figure 15(d), and Figure 15(e). The second pattern was that the impeller became unstable around the S2 condition, but regained stability when the flow rate further reduced, as shown in Figure 15(a), Figure 15(c), and Figure 15(f).

The variation trend of the stage SP was highly consistent with that of the impeller SP, with both curves showing similar shape. The difference was that the stage tended to become unstable earlier than the impeller. Considering that the diffuser remained unstable over almost the entire operating range, this indicated that the stage stability was primarily governed by the impeller. When the impeller stability reduced, the stage stability deteriorated accordingly. The volute SP curves showed negligible differences among all three geometry configurations, suggesting that the volute stability was not influenced by the minor geometry variations upstream in this study.

4.2. Correlation with Experimental Observations

Recalling the observations in Figure 8, it was found that there was a strong correlation between the experimentally measured compressor instability behavior and CFD predicted impeller SP value. Figure 15 also compares the experimentally observed compressor behavior, i.e., the CV value of inlet Δp, which is presented by the scatter points. A sudden increase in this CV value denotes the onset of compressor instability. A CV value greater than 40% (for case B_103%, it was set to 45%) was taken as the threshold for deep surge, while a CV value slightly below that threshold was associated with mild surge. This threshold was chosen on the basis of the extensive tests undertaken by Cummins Components & Software.

When the impeller SP value approached zero (or became positive), the CV of inlet Δp rose sharply to a value slightly below 40%, indicating the onset of the mild surge. Two scenarios can be observed later:

- If the impeller SP value subsequently reduced (the impeller stability recovered), the compressor exited mild surge, forming a surge island. This is corresponding to TYPE A instability behavior (Figure 8(a), Figure 8(c), and Figure 8(f)), as shown in Figure 15(a), Figure 15 (c), and Figure 15 (f).
- If the impeller SP value did not reduce after approaching zero or continued to increase, the mild surge persisted until the occurrence of the deep surge. This is corresponding to TYPE B instability behavior (Figure 8(b), Figure 8(d), and Figure 8(e)), as shown in Figure 15(b), Figure 15 (d), and Figure 15 (e).

In summary, the instability behavior of the studied compressor stages was mainly influenced by the impeller stability. When the impeller was unstable, the studied compressor stages experienced mild surge. It should be noted that, while the relatively large MFP increments in Figure 15 may introduce uncertainties in the quantitative evaluation of SP parameters, the aim of Figure 15 is to qualitatively illustrate the correlation between impeller instability characteristics and the onset of compressor mild surge. Therefore, this limitation has little impact on the conclusion drawn.

4.3. Discussion

The mechanisms by which the impeller stability recovers after deterioration and the formation of the surge island are discussed.

Figure 16 compares the circumferentially area-averaged streamlines on the impeller meridional surface of case B_100% under different operating conditions, obtained using the previously developed CFD model [28,30]. The locations of the ported shroud downstream slot, main blade leading edge and splitter leading edge are given. The streamlines are overlaid with contours of circumferentially area-averaged relative Mach number. At the S2 condition where the impeller stability became the worst, denoted by the impeller SP value reaching its maximum, a recirculating bubble was formed near the shroud side at the splitter blade leading edge. This recirculating bubble was identified as one of the sources of impeller instability [12]. As pointed out by Lin et al. [39], when the recirculating bubble extended towards the splitter blade leading edge as mass flow rate decreased, it introduced negative effects of preswirl and preheating. The swirl brought by the recirculating bubble had limited contribution to the reduction of the impeller incidence losses but reduced the work input. The local total temperature rise due to the preheating was equivalent to the power consumption of the recirculating bubble. Both exerted adverse influences on the compressor stability, triggering the mild surge.

With further reduction of the flow rate, the recirculating bubble grew primarily in the streamwise direction. When the recirculating bubble extended upstream to meet the downstream bleed slot of the ported shroud, it was partially drawn into the bleed slot. This suppressed the growth of the recirculating bubble and extracted some low-momentum flow, thereby enabling the impeller to regain its stability. As a result, the compressor exited the mild surge, leading to the formation of a surge island.

For cases where surge island did not appear, such as B_103%, the corresponding circumferentially area-averaged streamlines on the meridional surface are given in Figure 17. At the S1 condition (the MFP of S1 condition at 103% speed was higher than at 100% speed), the recirculating bubble extended upstream but did not reach the downstream bleed slot of the ported shroud. Consequently, the destabilizing effect of the recirculating bubble was not mitigated, thus the impeller stability was not recovered, and the compressor persisted in the mild surge state.

To the authors' knowledge, this is the first time that the interaction between the impeller exducer shroud endwall recirculating bubble and the bleed slot of the ported shroud has been presented. In addition to identification of this critical interaction, the underlying mechanisms of different surge behaviors of turbocharger centrifugal compressors with ported shroud configurations have been interpreted. This interpretation should be further explained in conjunction with the conclusion drawn in the authors' previous investigation, where the dominant component of compressor instability switched over at critical speedline [28]. For the B configuration, the compressor stage switched to diffuser dominated instability at somewhere between 100% and 103% speed. For impeller dominated instability cases (e.g., B_100%, R_100% and R_103%), the common feature was that the impeller stability became the worst near S2 condition and the whole stage entered mild surge. As the mass flow rate further reduced, the recirculating bubble at the exducer shroud was extracted when it extended sufficiently upstream to the downstream bleed slot of the ported shroud. This led to the recovery of the impeller stability, indicating that the impeller had the potential to operate stably at lower mass flow rates.

For the diffuser dominated instability cases (e.g., B_103%), once the impeller stability deteriorated and triggered the mild surge, it would theoretically be possible for the recirculating bubble at exducer shroud to extend upstream to the downstream bleed slot of the ported shroud and be removed, thereby restoring the impeller stability. However, this was not observed. The reason was that the diffuser reached its stability limit earlier,

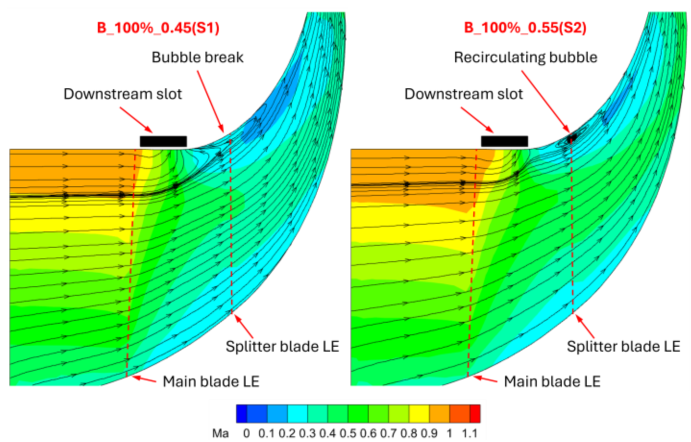

Figure 16: Circumferentially averaged meridional streamlines for B_100%

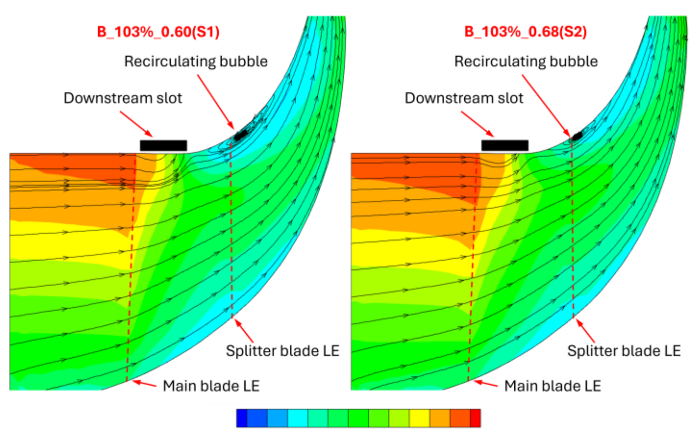

Figure 17: Circumferentially averaged meridional streamlines for B_103%

initiating the overall stage instability. Although the impeller itself still had the potential to operate at lower mass flow rates, the premature destabilization of the diffuser constrained the whole compressor stage, preventing further stable operation under lower mass flow rates. This phenomenon that the dominant instability component was shifted from the impeller to the diffuser as the rotating speed increased, was also observed by Zhang et al. [40].

5. CONCLUSIONS AND FUTURE WORK

This study has conducted experimental investigations on three ported shroud equipped turbocharger centrifugal compressors with local geometry variations in ported shroud strut length and diffuser recess size. The experiments included overall stage performance characterization, interstage static pressure measurements, and dynamic pressure measurements during the throttling process towards the surge boundary. Some conclusions are drawn below:

1. Minor geometry variations in non-core components of the studied compressor had a negligible influence on the overall aerodynamic performance close to design point. However, the performance map width can be significantly affected in some cases.
2. The measured interstage static pressures validated the accuracy and reliability of the previously developed high-fidelity unsteady CFD model. The discrepancy between numerical predictions and experimental measurements decreased progressively towards the downstream components of the stage.
3. The dynamic pressure measurements revealed two types of compressor instability behaviors: (i) TYPE A: a mild surge island appeared before deep surge; (ii) TYPE B: a mild surge followed by a deep surge. No evidence of rotating stall was observed for the studied compressors. Instead, a high-frequency signal (~80% IPF) was observed in the diffuser at the onset of mild surge, and persisted until deep surge occurred.
4. The onset of the mild surge was found to be closely associated with the variation of impeller stability. Mild surge occurred when the impeller stability parameter (SP) value approached zero, which was attributed to the growth of the recirculating bubble at the impeller exducer shroud endwall. For some cases (relatively low speeds), further reduction in mass flow rate led to a recovery of impeller stability and the exit of mild surge, forming a surge island. The underlying mechanism was that as the recirculating bubble extended upstream, it was removed when reaching the bleed slot of the ported shroud, consequently restoring the impeller stability.

To the authors' best knowledge, this investigation is the first study to present the interaction between the recirculating bubble at the impeller exducer shroud endwall and the ported shroud bleed slot. The underlying mechanisms of different surge behaviors of centrifugal compressors with ported shroud configurations have also been clarified. Building upon this understanding, future work may focus on exploiting this insight for more stable centrifugal compressor designs. Potential directions include optimizing the location of the ported shroud bleed slot to enable effective removal of the recirculating bubble at the impeller exducer shroud endwall, tailoring the shroud contour to mitigate or delay the development of the exducer shroud endwall recirculating bubble, or improving diffuser stability at high rotational speeds, where the diffuser triggered the stage instability before the recirculating bubble extended to the bleed slot of the ported shroud for removal.

ACKNOWLEDGEMENTS

The authors gratefully acknowledge Cummins Components & Software for providing research support and permission to publish this work. Acknowledgement is extended to Irish Centre for High-End Computing (ICHEC) for the provision of computational facilities and support, and to Ansys Inc for the use of their software. The author would also like to thank China Scholarship Council (No. 202006280008) for financially supporting Yiming Liu's PhD study at Trinity College Dublin.

REFERENCES

[1] Trébinjac, I., Bulot, N., Ottavy, X., and Buffaz, N., 2011, "Surge Inception in a Transonic Centrifugal Compressor Stage," ASME paper No. GT2011-45116.

[2] Stuart, C., Spence, S., Teichel, S., and Starke, A., 2021, "Experimental and Numerical Assessment of the Impact of an Integrated Active Pre-Swirl Generator on Turbocharger Compressor Performance and Operating Range," Energies, **14**(12), p. 3537.

[3] Van den Braembussche, R., 2019, *Design and Analysis of Centrifugal Compressors*, ASME Press, New York.

[4] Cumpsty, N.A., 2004, *Compressor Aerodynamics*, Krieger Publishing, Malabar, FL.

[5] Greitzer, E.M., 1976, "Surge and Rotating Stall in Axial Flow Compressors—Part I: Theoretical Compression System Model," ASME J. Eng. Power, **98**(2), pp. 190–198.

[6] Hansen, K.E., Jørgensen, P., and Larsen, P.S., 1981, "Experimental and Theoretical Study of Surge in a Small Centrifugal Compressor," ASME J. Fluids Eng., **103**(3), pp. 391–395.

[7] Zhang, M., Zheng, X., Huang, Q., and Sun, Z., 2019, "A Novel One-Dimensional–Three-Dimensional Coupled Method to Predict Surge Boundary of Centrifugal Compressors," ASME J. Eng. Gas Turbines Power, **141**(7), p. 071012.

[8] Huang, Q., Zhang, M., and Zheng, X., 2019, "Compressor Surge Based on a 1D-3D Coupled Method – Part 1: Method Establishment," Aerosp. Sci. Technol., **90**(2019), pp. 342–356.

[9] Toyama, K., Runstadler, P.W., and Dean, R.C., 1977, "An Experimental Study of Surge in Centrifugal Compressors," ASME J. Fluids Eng., **99**(1), pp. 115–124.

[10] Dean, R.C., and Young, L.R., 1977, "The Time Domain of Centrifugal Compressor and Pump Stability and Surge," ASME J. Fluids Eng., **99**(1), pp. 53–59.

[11] Zhao, B., Huang, C., Zhang, Z., Cui, W., and Zhou, T., 2025, “Experimental Study on the Effects of Compressor Rotational Speed on Surge Characteristics: Spatial and Temporal Frequencies,” Aerosp. Sci. Technol., **157**(2025), p. 109854.

[12] Manabe, K., Furukawa, M., Yamada, K., and Kusano, K., 2025, “Experimental and Numerical Analyses of Mild Surge in a Transonic Centrifugal Compressor With a Vaneless Diffuser,” J. Fluid Sci. Technol., **20**(1), p. 109854.

[13] Zheng, X., and Liu, A., 2015, “Experimental Investigation of Surge and Stall in a High-Speed Centrifugal Compressor,” J. Propul. Power, **31**(3), pp. 815–825.

[14] Zheng, X., Sun, Z., Kawakubo, T., and Tamaki, H., 2017, “Experimental Investigation of Surge and Stall in a Turbocharger Centrifugal Compressor With a Vaned Diffuser,” Exp. Therm. Fluid Sci., **82**, pp. 493–506.

[15] Sun, Z., Zheng, X., and Kawakubo, T., 2018, “Experimental Investigation of Instability Inducement and Mechanism of Centrifugal Compressors With Vaned Diffuser,” Appl. Therm. Eng., **133**, pp. 464–471.

[16] Lin, Y., Niu, Z., and Zheng, X., 2023, “Two-Regime Surge Mechanism in Centrifugal Compressors,” J. Propul. Power, **39**(2), pp. 190–201.

[17] Zheng, X., and Liu, A., 2015, “Phenomenon and Mechanism of Two-Regime-Surge in a Centrifugal Compressor,” ASME J. Turbomach., **137**(8), p. 081007.

[18] Zhao, B., Zhou, T., and Yang, C., 2023, “Experimental Investigations of Centrifugal Compressor Surge Noise,” ASME J. Turbomach., **145**(8), p. 081014.

[19] Fisher, F.B., 1988, “Application of Map Width Enhancement Devices to Turbocharger Compressor Stages,” SAE Trans., **97**, pp. 1303–1310.

[20] He, X., and Zheng, X., 2019, “Roles and Mechanisms of Casing Treatment on Different Scales of Flow Instability in High Pressure Ratio Centrifugal Compressors,” Aerosp. Sci. Technol., **84**(2019), pp. 734–746.

[21] Sivagnanasundaram, S., Spence, S., and Early, J., 2014, “Map Width Enhancement Technique for a Turbocharger Compressor,” ASME J. Turbomach., **136**(6), p. 061002.

[22] Tamaki, H., 2009, “Experimental Study on Surge Inception in a Centrifugal Compressor,” Int. J. Fluid Mach. Syst., **2**(4), pp. 409–417.

[23] Liu, A., and Zheng, X., 2013, “Methods of Surge Point Judgment for Compressor Experiments,” Exp. Therm. Fluid Sci., **51**, pp. 204–213.

[24] Liśkiewicz, G., Kulak, M., Sobczak, K., and Stickland, M., 2020, “Numerical Model of a Deep Surge Cycle in Low-Speed Centrifugal Compressor,” ASME J. Turbomach., **142**(12), p. 121005.

[25] Liśkiewicz, G., Horodko, L., Stickland, M., and Kryłłowicz, W., 2014, “Identification of Phenomena Preceding Blower Surge by Means of Pressure Spectral Maps,” Exp. Therm. Fluid Sci., **54**, pp. 267–278.

[26] SAE, 2022, “Turbocharger Gas Stand Test Code,” Society of Automotive Engineers, Warrendale, PA. Standard No. J1826_202204.

[27] Whittlesea, M., and Roberts, E., 2016, “Turbo Charger Compressor Inlet and Outlet Pipe Length and Volume, and the Effects on the Characteristics and Location of Surge,” 12th International Conference on Turbochargers and Turbo-Charging, May 17-18, London, IMechE, Paper No. 4.

[28] Liu, Y., Spence, S., Horsley, J., Mann, S., and Stuart, C., 2025, “Insights Into Turbocharger Centrifugal Compressor Stability Using High-Fidelity Computational Fluid Dynamics and a Novel Impeller Diffusion Factor,” ASME J. Turbomach., **147**(4), p. 041003.

[29] Chen, H., and Lei, V.-H., 2013, “Casing Treatment and Inlet Swirl of Centrifugal Compressors,” ASME J. Turbomach., **135**(4), p. 041010.

[30] Liu, Y., Spence, S., Sandford, G., Mann, S., McMath, D., and Stuart, C., 2025, “Characterization of Centrifugal Compressor Vaneless Diffuser Performance and Stability Using High-Fidelity Computational Fluid Dynamics,” Phys. Fluids, **37**(11), p. 116132.

[31] Harris, F.J., 1978, “On the Use of Windows for Harmonic Analysis With the Discrete Fourier Transform,” P. IEEE, **66**(1), pp. 51–58.

[32] He, X., and Zheng, X., 2018, “Flow Instability Evolution in High Pressure Ratio Centrifugal Compressor With Vaned Diffuser,” Exp. Therm. Fluid Sci., **98**, pp. 719–730.

[33] Casey, M., and Robinson, C., 2021, *Radial Flow Turbocompressors: Design, Analysis, and Applications*, Cambridge University Press, UK.

[34] Stuart, C., Spence, S., Filsinger, D., Starke, A., and Kim, S.I., 2018, “Characterizing the Influence of Impeller Exit Recirculation on Centrifugal Compressor Work Input,” ASME J. Turbomach., **140**(1), p. 011005.

[35] Dean, R.C., 1974, “The Fluid Dynamic Design of Advanced Centrifugal Compressors,” Lecture Notes, Von Karman Institute, Brussels, pp. 68–69.

[36] Japikse, D., 1987, “A Critical Evaluation of Three Centrifugal Compressors With Pedigree Data Sets: Part 5—Studies in Component Performance,” ASME J. Turbomach., **109**(1), pp. 1–9.

[37] Liu, X., and Jin, H., 2025, “Effect of Different Bleed Slot Positions and Negative Pre-Swirl Vanes on the Performance of Centrifugal Compressor With Recirculation Casing Treatment,” Phys. Fluids, **37**(2), p. 026124.

[38] Hunziker, R., and Gyarmathy, G., 1994, “The Operational Stability of a Centrifugal Compressor and Its Dependence on the Characteristics of the Subcomponents,” ASME J. Turbomach., **116**(2), pp. 250–259.

[39] Lin, Y., Fan, T., and Zheng, X., 2021, “Roles of Recirculating Bubble on the Performance of Centrifugal Compressors,” Aerosp. Sci. Technol., **118**(2021), p. 107073.

[40] Zhang, H., Yang, C., Zhao, B., Zhao, W., Hu, C., Wang, W., Gao, J., and Sun, S., 2023, “Experimental Investigation of Characteristics of Instability Evolution in a Centrifugal Compressor,” Chinese J. Aeronaut., **36**(4), pp. 174–189.

